Evaluation of Clouds, Radiation, and Precipitation in CMIP6 Models Using Global Weather States Derived from ISCCP-H Cloud Property Data

GEORGE TSELIOUDIS,[a,b] WILLIAM B. ROSSOW,[c] CHRISTIAN JAKOB,[d] JASMINE REMILLARD,[a,e] DEREK TROPF,[a,e] AND YUANCHONG ZHANG[a,e]

[a] *NASA/GISS, New York, New York*
[b] *Department of Applied Physics and Applied Math, Columbia University, New York, New York*
[c] *Franklin, New York*
[d] *ARC Centre of Excellence for Climate Extremes, Monash University, Melbourne, Victoria, Australia*
[e] *SciSpace, New York, New York*

(Manuscript received 26 January 2021, in final form 8 June 2021)

ABSTRACT: A clustering methodology is applied to cloud optical depth (τ)–cloud top pressure (TAU-PC) histograms from the new 1° resolution ISCCP-H dataset to derive an updated global weather state (WS) dataset. Then, TAU-PC histograms from current-climate CMIP6 model simulations are assigned to the ISCCP-H WSs along with their concurrent radiation and precipitation properties to evaluate model cloud, radiation, and precipitation properties in the context of the weather states. The new ISCCP-H analysis produces WSs that are very similar to those previously found in the lower-resolution ISCCP-D dataset. The main difference lies in the splitting of the ISCCP-D thin stratocumulus WS between the ISCCP-H shallow cumulus and stratocumulus WSs, which results in the reduction by one of the total WS number. The evaluation of the CMIP6 models against the ISCCP-H weather states shows that, in the ensemble mean, the models are producing an adequate representation of the frequency and geographical distribution of the WSs, with measurable improvements compared to the WSs derived for the CMIP5 ensemble. However, the frequency of shallow cumulus clouds continues to be underestimated, and, in some WSs the good agreement of the ensemble mean with observations comes from averaging models that significantly overpredict and underpredict the ISCCP-H WS frequency. In addition, significant biases exist in the internal cloud properties of the model WSs, such as the model underestimation of cloud fraction in middle-top clouds and secondarily in midlatitude storm and stratocumulus clouds, that result in an underestimation of cloud SW cooling in those regimes.

KEYWORDS: Cloud forcing; Cloud retrieval; Data mining; Satellite observations; Climate models; Clouds; Model evaluation/performance

1. Introduction

Satellite observations of cloud properties have been used to evaluate climate models ever since the TIROS meteorological satellites, launched by NASA in the 1960s, provided the first remote retrievals of global cloud cover (e.g., Somerville et al. 1974). Two main objectives of those cloud evaluation efforts were to inform model developers of the deficiencies in the model cloud field so as to assist in improving cloud parameterizations in future model versions, and to increase our understanding of cloud-related processes that play key roles in cloud climate feedbacks. Originally cloud fraction was the only observational field available for evaluation; but since the advent of the International Satellite Cloud Climatology Project (ISCCP; Rossow and Schiffer 1991), the launch of microwave radiometers like SSMI (Ferraro et al. 1996) and active sensing instruments such as radars and lidars on *CloudSat* and *CALIPSO* (Stephens et al. 2008; Winker et al. 2009), additional cloud properties like top pressure, optical thickness, liquid water path, and vertical extent were included in the model evaluation comparisons. For a long while, those evaluations were based on comparisons of time- and space-mean cloud fields, often one at a time and independent from the coincident properties of the atmosphere (e.g., Hansen et al. 1983; Schmidt et al. 2006). These comparisons provided quantitative measures of the deficiencies of the properties of the simulated clouds but did not provide information on the connections between the properties of the cloud field and the coincident atmospheric state and processes. As a result, this type of analysis often did not provide modelers with sufficient leads to the components of the model parameterizations that could be responsible for the cloud property deficiencies, and did not provide information on the mechanics of cloud-related processes that could be responsible for cloud climate feedbacks.

This pointed to the need to develop more process-based model evaluation techniques, and several methods were developed with the aim to sample observational data into distinct regimes and evaluate model cloud properties within each regime. The regime definition methods that were applied can be divided into two broad categories. In the first category, one or more atmospheric parameters were used to derive a dynamic or thermodynamic regime in observations and models, and the model clouds were evaluated in that particular regime. Following this methodology, model clouds were evaluated, among others, in tropical and midlatitude ascending and descending motion regimes (Bony and Dufresne 2005; Tselioudis and Jakob 2002), in combined vertical motion/boundary layer

Corresponding author: George Tselioudis, george.tselioudis@nasa.gov

DOI: 10.1175/JCLI-D-21-0076.1

© 2021 American Meteorological Society. For information regarding reuse of this content and general copyright information, consult the AMS Copyright Policy (www.ametsoc.org/PUBSReuseLicenses).

stability regimes (Grise and Medeiros 2016), and in midlatitude storm composites (Bodas-Salcedo et al. 2014). These analyses put model cloud deficiencies in the context of atmospheric processes, showing for example that model boundary layer cloud cover was deficient in subsidence regimes in general (Bony and Dufresne 2005; Tselioudis and Jakob 2002) and in midlatitude cold air outbreaks in particular (Bodas Salcedo et al. 2014), and that this low cloud bias may be in part due to a stronger than observed dependence of model cloud formation on vertical velocity and a weaker than observed dependence on boundary layer stability (Grise and Medeiros 2016).

In the second regime definition category, data mining techniques such as cluster analysis or neural networks are applied to the cloud properties themselves in order to extract cloud-defined regimes, and the analysis of the atmospheric conditions is subsequently used to understand the regime behavior. A data mining technique used widely in cloud property analysis relies on the application of the *K*-means clustering algorithm (Anderberg 1973) on combined histograms of cloud optical depth (τ)–cloud top pressure (TAU-PC) from the ISCCP or the Moderate Resolution Imaging Radiospectometer (MODIS) datasets. The method was first applied to the 2.5°, 3-hourly ISCCP-D1 dataset for the region of the western Pacific (Jakob and Tselioudis 2003). It was then extended to the whole tropics in Rossow et al. (2005), and to the globe in Tselioudis et al. (2013). The derived cluster centroids represented distinct cloud type distributions characterized by distinct TAU-PC histograms, and were shown to relate to discrete atmospheric regimes that were termed weather states (WSs). Application of the same clustering method to MODIS TAU-PC histograms (Oreopoulos et al. 2014) produced a set of cloud regimes similar in nature to the ISCCP weather states. The ISCCP-D1 WSs were used in the evaluation of cloud simulations in the Climate Model Intercomparison Project phase 3 (CMIP3; Williams and Tselioudis 2007; Williams and Webb 2009) and phase 5 (CMIP5; Jin et al. 2017) families of models. The analysis of Williams and Webb (2009) showed large model spread and deficiencies in cumulus congestus (midlevel) and transition (shallow cumulus) clouds in the extratropics, at magnitudes similar to the previously identified model deficiencies in stratocumulus clouds in the tropics. This led to the more focused analysis of Bodas-Salcedo et al. (2014), who identified cold air outbreaks behind frontal zones in the Southern Oceans as a major regime of model cloud deficiencies. Similar deficiencies in CMIP5 model shallow cumulus clouds in North Atlantic cold air outbreaks was found in Rémillard and Tselioudis (2015). The analysis of Jin et al. (2017) found tendencies in the CMIP5 models to underestimate the occurrence of optically thin clouds and clouds with midlevel tops, and to perform better in the simulation of optically thick storm clouds.

In the past few years, two new sources of data have become available to the science community. First, a new 1° horizontal resolution version of the ISCCP cloud property products was introduced (ISCCP-H; Young et al. 2018). At the same time, the latest versions of climate models were used in the CMIP6 program to perform a suite of present and future climate simulations. The present study takes advantage of those new resources, by first applying the clustering methodology of Tselioudis et al. (2013) to the TAU-PC histograms of the ISCCP-H dataset, in order to derive an updated cloud-defined weather state dataset. Then, TAU-PC histograms from the output of the CMIP6 model simulations are assigned to the derived weather states along with their concurrent radiation and precipitation properties, with the objective to create model WS climatologies and to evaluate cloud, radiation, and precipitation properties in CMIP6 models in the context of the WSs.

2. Datasets and analysis method

a. *ISCCP-H 1° dataset*

A summary description of the new ISCCP-H products is provided by Young et al. (2018), with complete details in the Climate Algorithm Theoretical Basis Document (Rossow 2017). Overall, the ISCCP-H cloud property retrievals are very similar to the ISCCP-D ones, with only a few notable differences. Higher spatial resolution produces a more "U-shaped" distribution of cloud amount frequencies and hence, as also shown below, the frequency of occurrence of completely clear conditions increases and the total cloud cover for the cloud WSs increases. The only significant change in ISCCP-H cloud amount is a decrease by about 0.1 (absolute) over Antarctica in summertime because of the removal of the test on the 3.7-μm channel, which is not available over the whole record. Average cloud top pressures in both polar regions increase by 30–40 mb (1 mb = 1 hPa) in winter and decrease by about the same amount in summer relative to the ISCCP-D values, due mainly to the change in the ancillary atmospheric temperature profile dataset that is used (cloud top temperatures are nearly the same on average). There is an increase in the amount of high, thin clouds (identified in the summer where daylight is available), which appears to be consistent with *CALIPSO* observations. The final significant change in cloud properties is a decrease of the cloud top temperature threshold used to separate ice and liquid clouds to 253 K from 260 K, which reduces the relative amount of ice clouds in the ISCCP-H dataset.

b. *WS derivation through K-means clustering*

The method described in detail in Tselioudis et al. (2013) and previous papers (Jakob and Tselioudis 2003; Rossow et al. 2005) was also used here to perform the cluster analysis of the ISCCP-H TAU-PC histograms. The *K*-means clustering algorithm (e.g., Anderberg 1973) was applied to the cloud fraction vector formed from the histograms of PC-TAU for each 3-hourly, 1° ISCCP-H grid cell over the period July 1983–June 2015 to derive optimized PC-TAU clusters. Since TAU is only available during daytime in the ISCCP-H dataset, the derived clusters are also only available for 3-hourly daylight periods. In the cluster analysis, the "best" (optimum) cluster number K is determined objectively by a set of diagnostic checks, described in detail in Tselioudis et al. (2013). Briefly, the clustering algorithm is run in consecutive steps with K increasing by 1, and in every iteration statistical tests are carried out to check four criteria: whether the clustering procedure converges, whether this convergence is insensitive to the set of centroids used to initiate the algorithm, whether the dispersion of all the vectors

in each cluster is minimized, and finally whether a distinctly new centroid pattern has appeared when increasing K by 1 from the previous set of clusters. Note that grid points that are completely cloud free are not included in the cluster analysis process and form their own clear-sky category.

Based on the above criteria, the method is applied on the ISCCP-H TAU-PC histograms. The analysis produces a set of 10 cloud weather states as the most stable result, and the dataset and plots for the ISCCP-H weather states are archived and presented at http://isccp.giss.nasa.gov/wstates/hggws.html. The cluster analysis of the ISCCP-H data yields two pairs of WSs that include very similar TAU-PC histograms and geographical distributions, with the only difference between them being the mean optical thickness of the two cloud clusters involved. Specifically, the clustering algorithm produces an optically thinner and an optically thicker cirrus WS (WS3 and WS6 respectively in the original set) as well as an optically thinner and an optically thicker stratocumulus WS (WS9 and WS10), with both pairs having very similar geographical distributions. Since the present paper focuses on the evaluation of the performance of a large model ensemble in simulating the properties of the observational WSs, to achieve better clarity for the evaluation results it was decided to merge those two pairs into one cirrus and one stratocumulus WS (WS3 and WS8 respectively in the merged set). The merging is done by creating two new WSs that include all grid cells assigned to the optically thin and thick cirrus and stratocumulus WSs respectively and are represented by the weighted average PC-TAU histogram of the original WSs. This results in the set of the eight cloud WSs presented and used in this paper. Any studies that require a more detailed resolution of the cirrus and stratocumulus cloud fields, such as a more detailed model evaluation of those WSs, can be done by accessing the more detailed 10-cloud WS dataset that is archived in the ISCCP WS web page provided above.

c. Model evaluation through WS assignment

Climate model AMIP simulations of the twentieth century are evaluated in this study using the ISCCP-H weather states. The models that are used in the analysis are all the ones that provide output from the application of an ISCCP simulator package (Bodas-Salcedo et al. 2011), which derives daily TAU-PC histograms from model cloud parameters. A list of the CMIP6 models that are used, along with their horizontal and vertical resolutions is provided in Table 1. The majority of the models have horizontal resolutions close to the 1° resolution of the ISCCP-H dataset, with two models having resolutions closer to 2°. Note that when this resolution effect was tested by degrading the ISCCP-H data to 2° and repeating the WS assignment, the resulting WS dataset was almost identical with the 1° version, implying that the model resolution differences should not introduce discernable biases to the evaluation. To create a model WS climatology, each daily model TAU-PC histogram is assigned to the ISCCP-H WS with which it has the smallest Euclidian distance, and the derived model WS frequencies and cloud properties are evaluated against the corresponding ISCCP-H ones. To perform comparisons of compatible model-observations quantities, a modified ISCCP-H WS dataset is created through assignment of daily, rather than 3-hourly, ISCCP-H TAU-PC histograms to the WS centroids. The result of the transition to the daily ISCCP-H WSs is a significant reduction in the clear sky occurrence with smaller reductions in all high cloud-fraction WSs, and a corresponding significant increase in the fair weather WS and a smaller increase in the cirrus WS. Once model WSs are assigned to ISCCP-H WSs, model radiation and precipitation composites for each WS are constructed and evaluated against analogous ISCCP composites, which are derived using for radiation the ISCCP-FH dataset (available at https://isccp.giss.nasa.gov/projects/flux.html), and the CERES dataset (Loeb et al. 2018), and for precipitation the TRMM-3B42 (Huffman et al. 2007) dataset. Note that in order to map changes in the model cloud WS frequency and properties between the CMIP5 and CMIP6 model ensembles, the WS analysis is also performed on CMIP5 output of the previous generation of the analyzed CMIP6 models.

TABLE 1. CMIP6 models used in the WS analysis with horizontal resolution and vertical layering.

Model	Horizontal resolution (lat × lon)	Vertical layering
CESM2	0.94° × 1.25°	32 levels
CNRM-CM6-1	1.40° × 1.41°	91 levels
CNRM-ESM2-1	1.40° × 1.41°	91 levels
GFDL-CM4	2.0° × 2.5°	33 levels
GISS-E2-1-G	2.0° × 2.5°	40 levels
GISS-E3-G	1° × 1.25°	102 levels
HadGEM3-GC31-LL	1.25° × 1.875°	85 levels
IPSL-CM6A-LR	1.27° × 2.5°	79 levels
MRI-ESM2-0	1.12° × 1.125°	80 levels
UKESM1-0-LL	1.25° × 1.875°	85 levels

3. Results

a. Merged ISCCP-H weather states

Figure 1 shows the TAU-PC histograms of the eight cloud WSs derived from the cluster analysis of the 1° resolution ISCCP-H data and the subsequent merging (top), along with global maps of the relative frequency of occurrence (RFO) of each WS and of clear sky (bottom). The WS histograms are arranged as follows. The top three categories include high-top cloud WSs, namely optically thick tropical deep convective and anvil clouds (WS1-DCN), somewhat lower-top and optically thick midlatitude storm clouds (WS2-MDS), and optically thin high cirrus clouds (WS3-CIR). Those three high cloud categories occur 6.7%, 9.5%, and 15.9% of the time, respectively, and while the deep convective and storm cloud WSs are practically overcast, the cirrus WS has a cloud cover of about 80%. The latter may be in part due to the fact that the ISCCP satellite retrievals miss the thinnest cirrus clouds (Stubenrauch et al. 2013). The next two categories include polar clouds that show a mix of various top heights and optical thicknesses with an RFO of 3% and a cloud cover of 84.5% (WS4-PLR), and optically thick and nearly overcast middle-top clouds (WS5-MID) that occur 6.1% of the time. Then there is the fair-weather (WS6-FRW) category that has the lowest cloud cover (40%)

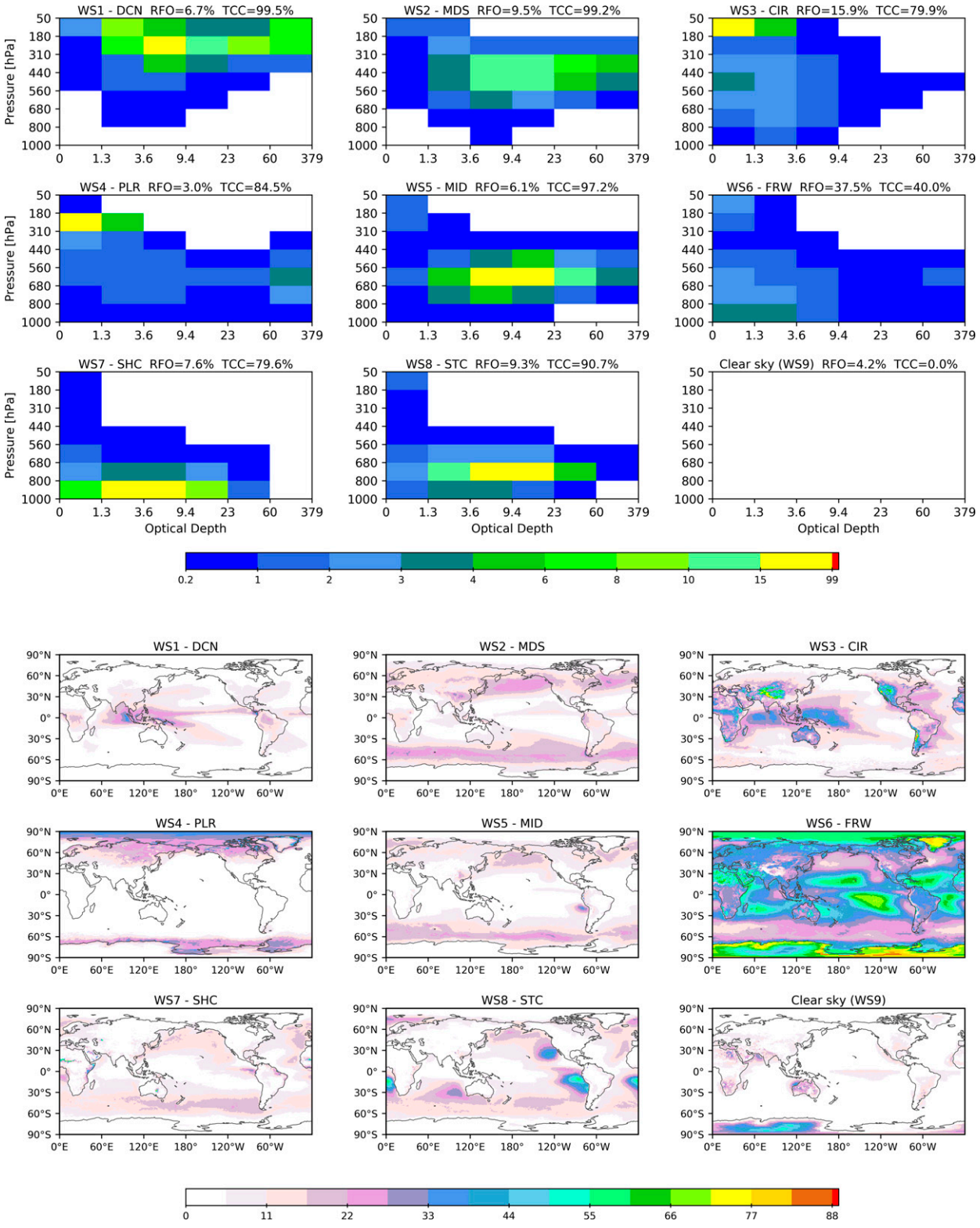

FIG. 1. (top) Cloud top pressure–cloud optical thickness (PC-TAU) histograms for the eight cloud weather states and a blank histogram (shown at bottom right) for clear sky. Noted on top of each histogram are the relative frequency of occurrence (RFO) and the total cloud cover (TCC). (bottom) Global RFO maps of the eight cloud WSs and of clear sky.

TABLE 2. ISCCP-H weather state mean values of cloud parameters.

	DCN	MDS	CIR	PLR	MID	FRW	SHC	STC
Avg PC (hPa)	242.6	433.6	316.3	395.6	606.9	645.1	840.1	725.5
Avg TAU	10.5	10.4	1.2	2.2	9.5	3.2	4	6.3
Total CF (%)	99.5	99.2	79.9	84.5	97.2	40	79.6	90.7

and the highest frequency of occurrence (37.5%), and includes mostly scattered thin cumulus and cirrus clouds. Finally, there are the two low-top cloud categories. The first includes optically thinner and lower cloud-top shallow cumulus clouds (WS7-SHC), which have a large cloud cover (79.6%) that indicates systemic organization rather than a scattered cloud field. The second includes optically thicker low clouds with larger cloud cover (90.7%) and higher cloud top, indicative of stratocumulus clouds (WS8-STC). The ninth weather state (WS9-CLR) represents completely cloud-free grid boxes, which occur 4.2% of the time and were not included in the clustering analysis. Table 2 lists the average cloud top pressure, cloud optical thickness, and cloud cover of all eight cloud WSs.

The WS RFO maps (Fig. 1, bottom) show that deep convective clouds (WS1) are concentrated primarily in the ITCZ/SPCZ region, with a small concentration in the entry regions of the northern midlatitude storm tracks near the west coasts of the Northern Hemisphere (NH) continents. Cirrus clouds (WS3) occur both in the ITCZ, with larger concentrations in the tropical west Pacific and Indian Oceans, and in the vicinity of large mountain ranges like the Himalayas, Rockies, and Andes. The midlatitude storm clouds (WS2) occur in the core of the midlatitude storm tracks, while the middle top (WS5) and the organized shallow cumulus (WS7) clouds occur primarily in the poleward and equatorward edges of the storm tracks, respectively. The polar clouds (WS4) are well confined in the polar regions, and the stratocumulus clouds (WS8) occur mostly off the western coasts of the main continents, with additional occurrence in the midlatitude storm tracks. The fair-weather cloud WS shows high populations in the middle of the tropical and subtropical ocean basins and in the polar regions.

The ISCCP-H WSs are very similar to the lower-resolution ISCCP-D WSs (Tselioudis et al. 2013), with only one significant difference: while the ISCCP-D analysis produced three stratocumulus WSs of low, medium, and high optical thickness, the ISCCP-H cluster analysis splits the low optical thickness stratocumulus WS between the shallow cumulus and the medium thickness stratocumulus WSs, thus producing two stratocumulus WSs of medium and high optical thickness and reducing the total number of WS by one. Note, however, that in the merged analysis presented in this paper the two ISCCP-H stratocumulus WSs were further combined into one WS8-STC. Furthermore, the ISCCP-H cluster analysis produces a polar WS that is much better confined to the polar regions than the corresponding one in the ISCCP-D analysis. Finally, due to its higher resolution, the ISCCP-H WS set has a 2% higher amount of cloud-free boxes than the ISCCP-D WS set and a little higher total cloud cover in all WS categories.

The vertical structure of the merged ISCCP-H WSs is shown in Fig. 2, derived from analysis of coincident retrievals from the *CloudSat*/*CALIPSO* radar/lidar active measurements. The independently derived vertical profiles from the active instruments fall well within the cloud type assumptions derived from the radiatively derived ISCCP-H TAU-PC histograms. They show that deep convection and midlatitude storm cloud WSs consist primarily of extensive cloud layers that cover the depth of the troposphere, cirrus clouds consist of thin high cloud layers, stratocumulus and shallow cumulus clouds consist of mostly isolated low cloud layers, and middle-top clouds consist both of layers that top in the middle troposphere and of coincident low and cirrus clouds, a situation that produces a midtroposphere radiative IR signature (cf. Jin and Rossow 1997). The radar/lidar confirm the presence of more high-top and fewer low-top clouds in the ISCCP-H polar WS than its ISCCP-D counterpart, due to both the better restriction of this WS to the polar regions and to an increase in ISCCP-H high cloud detections in that region. Some of the cirrus missed by ISCCP appears in the composite radar/lidar for WS9 (CLR). In general, the vertical cloud structures in Fig. 2 appear to be less of a mixture of cloud layers and to have more distinct layer structures than the equivalent ones for ISCCP-D (Tselioudis et al. 2013).

The WSs derived from the cluster analysis of the TAU-PC histograms are named after cloud types that are customarily associated with morphological cloud characteristics, often visible in satellite images. An attempt to associate the WSs to cloud morphological features observed in satellite images is shown in Fig. 3, where a grid of the derived WSs with their assigned number is overlaid on a visible image from the MODIS instrument on the *Aqua* satellite, for the case of a midlatitude storm system that covers most of the North Atlantic region. It can be seen that the cold and warm frontal conveyor belts of the storm are dominated by midlatitude storm WS2-MDS clouds, along with some embedded deep convective WS1-DCN clouds occurring mostly in the northern storm edge where the warm conveyor belt wraps around the low pressure center. The WSs occurring in the cold air outbreak region behind the front can be seen as a transition between two distinct regimes: 1) the regime in the northwestern region of the storm, where the continental cold/dry air flows over the warm Gulf Stream waters, and which is dominated by nearly overcast middle-top WS5-MID and stratocumulus WS8-STC clouds, and 20 the regime farther downstream, where, as the thicker cloud deck breaks up and cloud cover decreases, the region is dominated by shallow cumulus WS7-SHC. The prefrontal maritime and postfrontal continental regions are dominated by fair-weather WS6-FRW clouds. Note that the figure is a compilation of two *Aqua* overpasses that took place within the 3-h window of the ISCCP observation, so there is some uncertainty in the observation time and exact time correspondence of each grid box

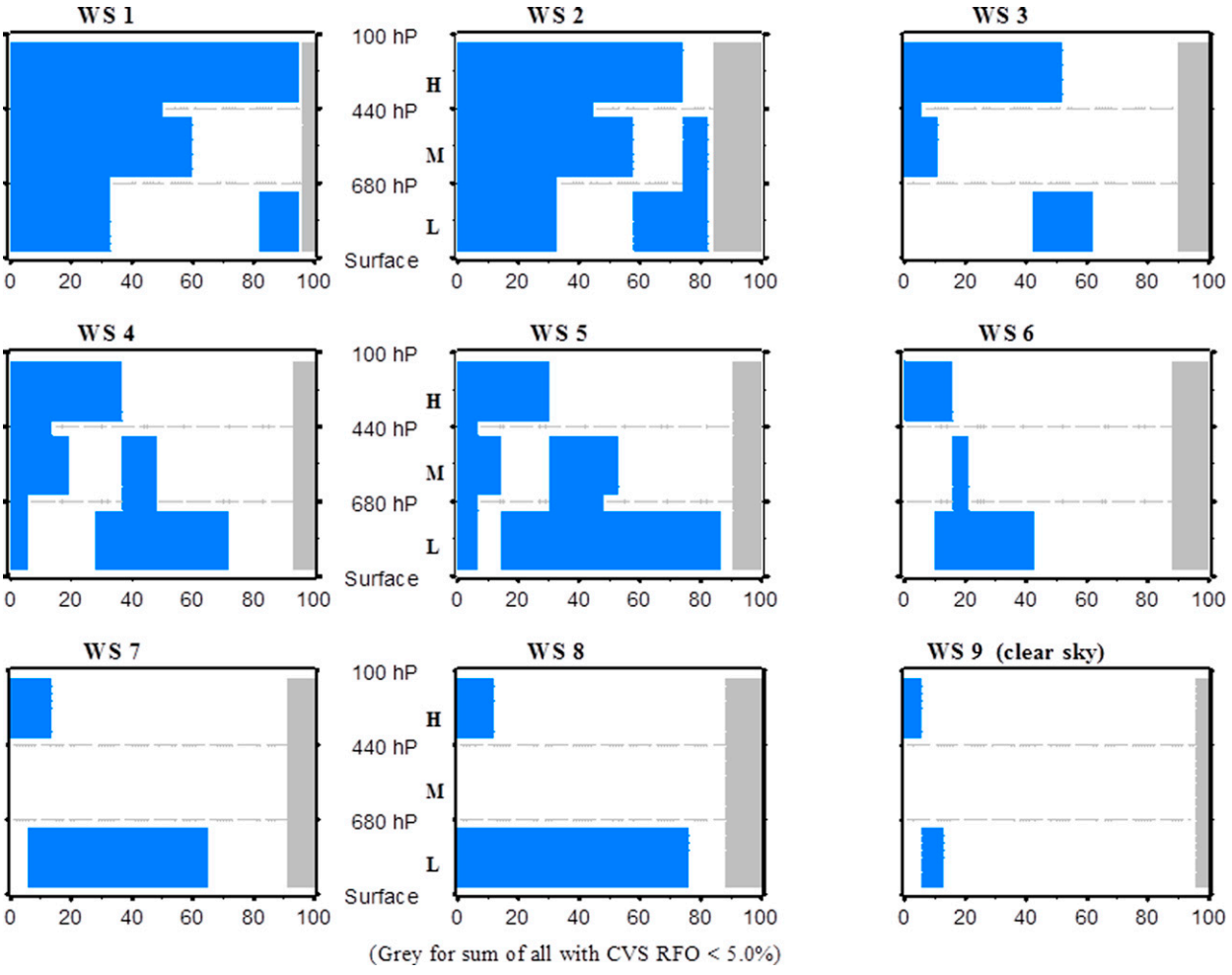

FIG. 2. Cloud vertical structure (CVS) distributions for the eight cloud WSs and for clear sky, derived from *CloudSat*/*CALIPSO* retrievals. The blue bars indicate cloud presence in a vertical layer, and the width of each CVS bar indicates the frequency of occurrence of this CVS in the particular WS [see Fig. 4 of Tselioudis et al. (2013) for CVS definitions]. The white bar (space) indicates clear sky, and the gray bar represents the sum of all CVSs that occur less than 5% of the time.

with ISCCP cannot be expected. However, the figure demonstrates that the cloud types defined through the cluster analysis of the ISCCP TAU-PC histograms correspond closely with the dynamic regimes where those cloud types are expected to occur (cf. Lau and Crane 1995; Tselioudis et al. 2013).

b. Weather state dynamical characteristics

The WS variability in the context of the conveyor belts of a midlatitude storm depicted in Fig. 3 shows the strong dynamical controls on cloud property distribution. Model cloud deficiencies often occur in specific dynamic regimes, and clouds occurring in postfrontal cold air outbreaks have been identified as primary sources of model error in previous evaluations of CMIP3 and CMIP5 models (e.g., Williams and Webb 2009; Bodas-Salcedo et al. 2014). These low and middle top cloud structures have distinct radiative characteristics and occur when particular combinations of dynamic and thermodynamic conditions are present. In addition, getting the atmospheric heating and cooling by the characteristic WS right is crucial to the feedbacks on the atmospheric dynamics (cf. Rossow et al. 2016). To start resolving the distinct dynamic conditions under which the different WSs are formed, Fig. 4 shows the distribution of midtropospheric vertical velocity for each WS by plotting the WS box-and-whisker diagrams of ERA-Interim 500-mb vertical velocity (Dee et al. 2011). The vertical velocity distributions show a regular progression, going from strong ascending motion in convective and storm clouds to a mixed motion regime in cirrus and middle top clouds, and then to a descending regime in low top clouds, similar to the progression found for the ISCCP-D WSs in Tselioudis et al. (2013). However, Fig. 4 shows that groupings of WSs have similar vertical velocity distributions, with small differences only in the distribution width or the length of the tails. Stratocumulus and shallow cumulus clouds, for example, both occur primarily in moderate descending motion and have distribution tails reaching into the strong descending and weak ascending motion, with shallow cumulus clouds showing greater width and tail variability.

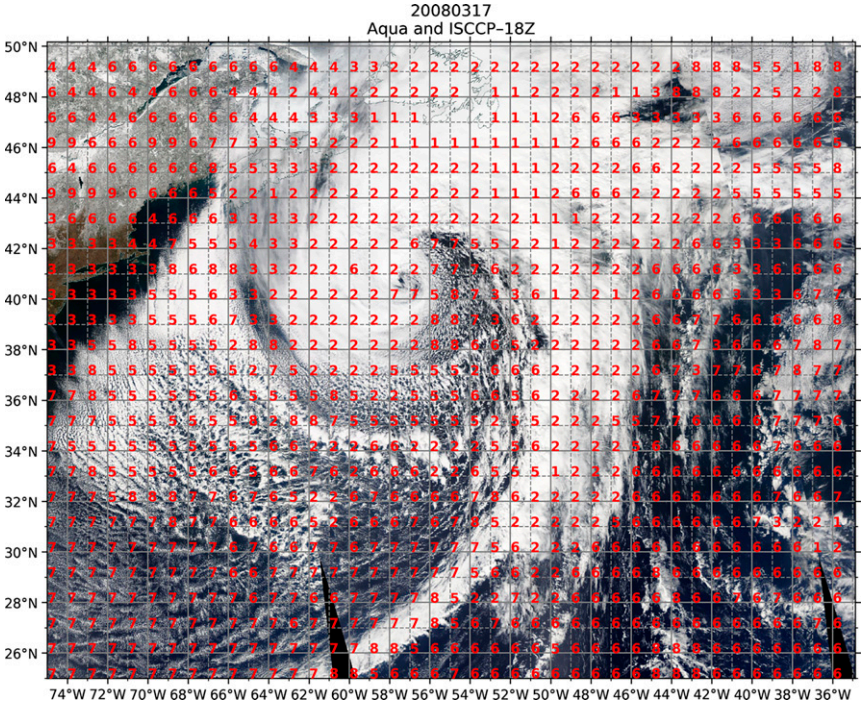

FIG. 3. A MODIS-*Aqua* visible channel image over the North Atlantic superimposed on a grid that indicates with a numerical value the coincident ISCCP-H weather state at the same time span and location.

Since vertical motion by itself only resolves broad differences between ascending and descending cloud regimes, a second layer of dynamical complexity can be added by looking at the differences in WS horizontal winds. Figure 5 shows wind roses of the 850-mb wind from ERA-Interim (Dee et al. 2011) for each WS, illustrating wind direction and speed together with the relative occurrence of each wind subdivision. Note that Southern Hemisphere meridional wind direction has been reversed so that in the plot northerly wind always implies an equatorward direction. At the top of each plot, the label shows the percentage of time that each WS occurs in the tropical, midlatitude, and polar regions. Most WS wind roses include one dominant wind direction regime, but several WSs show a second significant regime as well. Overall, the more tropical WSs (DCN, CIR, FRW) occur under the influence of easterly trade winds, but deep convection has a significant southwesterly wind component coming potentially from convection embedded in midlatitude storm systems and from convection formed during the summer Asian monsoon. The more midlatitude WSs (MDS, MID) and the polar WS are dominated by westerly winds characteristic of the baroclinic jet regime, with the midlatitude storm WS showing a southwesterly component typical of the cold-frontal conveyor belt and the middle top WS showing a northwesterly component typical of the postfrontal cold air outbreak circulation. The stratocumulus and shallow cumulus WSs show almost equal frequency of occurrence in tropical and midlatitude regions, and both include a prominent northeasterly wind component characteristic of the trade wind regime and a secondary but still significant northwesterly component characteristic of the postfrontal circulation.

This further separation of WSs in horizontal wind regimes indicates that stratocumulus and shallow cumulus cloud structures, with similar radiative characteristics and even dynamical environments as far as the vertical motion field is concerned, can occur in two distinct dynamic regimes as defined by the

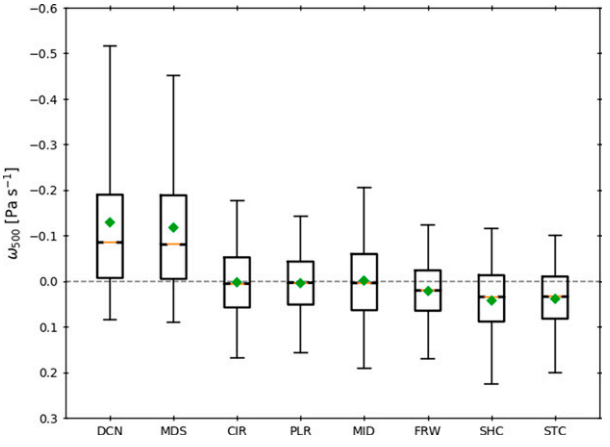

FIG. 4. Box-and-whisker diagram of ERA-Interim 500-mb vertical velocity distributions for the eight cloud WSs. The line represents the median, the rhombus represents the mean, the box represents the 75th percentile, and the bar represents the 95th percentile of each distribution.

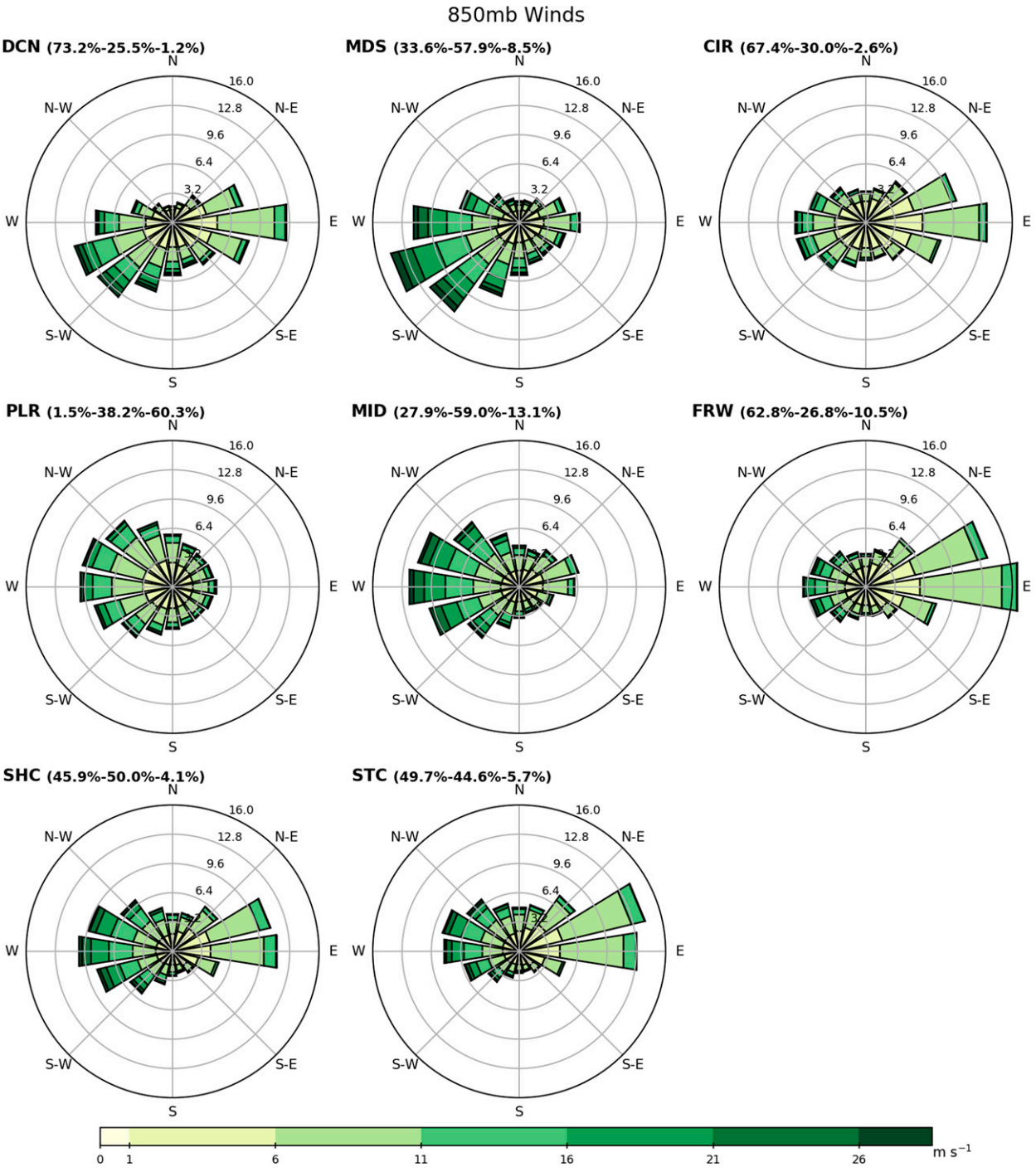

FIG. 5. Wind rose diagrams for the eight cloud WSs, from ERA-Interim 850-mb wind data. The length of each ''spoke'' around the circle indicates the fraction of time that the wind blows from a particular direction, noted on the circles. Colors along the spokes indicate categories of wind speed, noted on the color bar at the bottom of the plot. At the top of each plot, the label shows the percentage of time that each WS occurs in the tropical (30°S–30°N), midlatitude (30°–60°N/S), and polar (60°–90°N/S) regions.

horizontal wind: in cold air outbreaks behind frontal systems and in easterly trade wind regimes. This implies that clouds in those WSs can be formed through two distinct stratocumulus-to-shallow cumulus transition mechanisms; one in which cloud formation is driven by surface latent heating and boundary layer instability and cloud breakup by precipitation onset (Fig. 3) and the other in which cloud formation is driven by cloud-top radiative heating and turbulence and cloud break-up

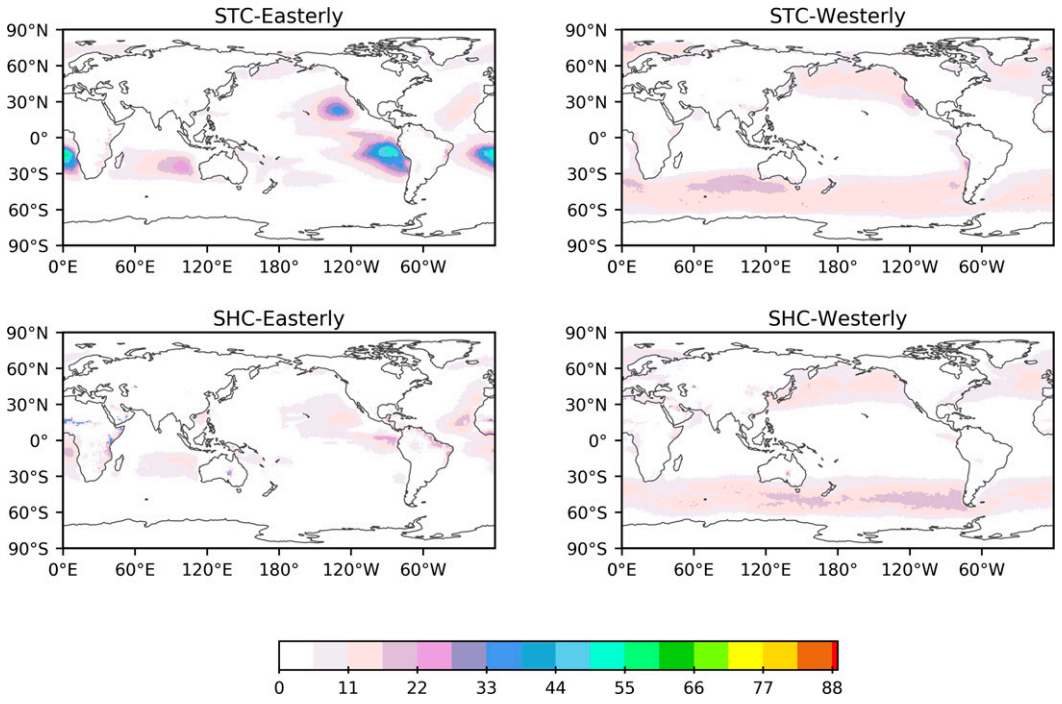

FIG. 6. Global maps of the relative frequency of occurrence (RFO) of the (top) stratocumulus and (bottom) shallow cumulus WSs, separately for their (left) easterly and (right) westerly wind components.

by dry air entrainment. To distinguish between the two different stratocumulus and shallow cumulus dynamic regimes, the STC and SHC WSs are split into their westward and eastward horizontal wind components using the 850-mb wind plotted in Fig. 6. The resulting TAU-PC histograms (not shown) are very similar, with slightly higher optical thickness for the westward components, and the global RFO numbers are split almost evenly between the easterly and westerly components (4.9%–4.4% for STC, 3.6%–4% for SHC). The resulting RFO global maps are shown in Fig. 6, for the STC WS at the top and the SHC WS at the bottom. It can be seen that the splitting by the horizontal wind regime clearly separates the midlatitude from the tropical components of the stratocumulus and shallow cumulus WSs, thus making possible more targeted studies of the mechanisms involved in the two different cloud transitions.

c. *CMIP6 model cloud evaluation*

The relative frequency of occurrence (RFO) of the merged H-WSs from the ensemble of CMIP6 model AMIP simulations that provided the necessary TAU-PC histograms at daily resolution is shown in Fig. 7, together with the daily merged ISCCP-H WS RFO. Note that the model WSs are derived through assignment of each model TAU-PC histogram to the ISCCP WS with which it has the smallest Euclidian distance. The figure also shows the model ensemble mean, and with smaller symbols the WS distributions of an ensemble of CMIP5 models that contains the earlier versions of the same models included in the CMIP6 ensemble. For most WSs the ensemble mean RFO of the CMIP6 models falls within or just outside the limits of the observational uncertainty, with the notable exception of the clear sky fractions that are significantly higher in all models than in the satellite retrievals. The main reason for this difference is that over the Sahara and Arabian deserts the models tend to simulate frequent daylight clear-sky conditions while the satellites retrieve mostly fair-weather clouds. The good agreement of the model ensemble mean with observations shown in Fig. 4 is in several WSs the result of a wide spread of model RFO values located on either side of the observed value. Moreover, systematic biases, with all or most models biased in the same direction, exist in several WSs. The most pronounced systematic bias occurs in the shallow cumulus WS, where all but two models significantly underestimate the RFO amount. Smaller systematic RFO biases exist in fair weather and deep convective clouds, where most CMIP6 models fall below the ISCCP line. The underestimate of shallow cumulus clouds found in both CMIP6 and CMIP5 ensembles has also been noted in several previous analyses of CMIP5 simulations (e.g., Bodas-Salcedo et al. 2014; Rémillard and Tselioudis 2015) and was attributed to cloud underestimation in cold air outbreaks behind midlatitude frontal systems, while the underestimate of midlevel cloud was also found in the WS analysis of CMIP5 models of Jin et al. (2017).

As noted before, in addition to the systematic model biases, in several WSs the models tend to fall into two contrasting groups that severely underestimate and severely overestimate respectively the ISCCP-H WS RFO values. To quantify the CMIP6 model RFO bias spread in a way that avoids the positive and negative bias cancellations of the averaging Table 3 shows the WS RFO absolute deviation (in %) of the CMIP6

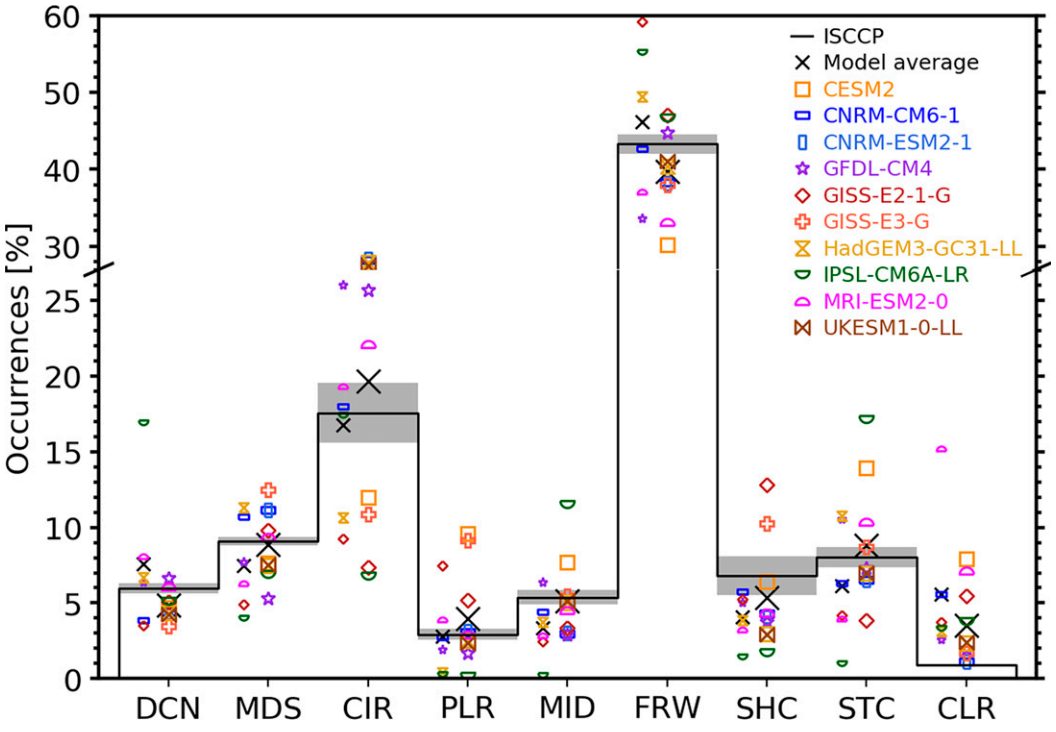

FIG. 7. Relative frequency of occurrence of the eight cloud WSs and clear sky, from the ISCCP-H dataset (solid line) and the AMIP twentieth-century simulations of the CMIP6 and CMIP5 models (model symbols are indicated in the label). The gray bar around the line indicates the ISCCP-H interannual variability. The larger symbols on the right column correspond to the CMIP6 versions of the models and the smaller symbols on the left side to the CMIP5 versions of the models. The X sign is the mean of each model ensemble.

and CMIP5 model ensembles from the observed RFO, normalized by the observed RFO value. It can be seen that in the CMIP6 model ensemble the absolute WS RFO deviation is above 30% of the observational value for the cirrus, polar, stratocumulus, midlevel, and shallow cumulus WSs, implying that the model ensemble mean agreement with the observations often results from the averaging of significant contrasting biases. Compared to the CMIP5 ensemble, the CMIP6 models show RFO absolute deviation values in five cloud WSs that are smaller than the CMIP5 model ones, thus resulting in a smaller overall mean deviation and implying an improved representation of the WS RFO distribution by the CMIP6 models.

As noted before, the WS assignment for the models is done through closest association of the model PC-TAU histograms with the ISCCP WSs, implying that the resulting model WSs can still differ significantly in their cloud cover, optical thickness, or cloud top pressure values or their geographical distribution from the ISCCP WS to which they are assigned. Those differences, which can result in model radiation or precipitation biases even in cases of correct WS RFO representations, are examined in Fig. 8. The figure shows for each WS the model difference in (from top) mean cloud fraction, mean optical depth, and mean cloud top pressure from the corresponding ISCCP WS, and (bottom) the RMS difference of WS geographical pattern derived through differencing of the WS RFO maps of each model from the corresponding ISCCP maps. The CMIP5 model ensemble mean is also plotted on all the panels. It can be seen that with the only major exception of the shallow cumulus WS, CMIP6 models tend to underestimate WS cloud fraction by about 4%–6%, and the underestimation is smaller than in CMIP5 models for most WSs. This difference, however, can be in part due to the generally lower horizontal model resolutions in the CMIP5 ensemble. At the same time, model cloud optical depth is higher than ISCCP in five WSs, the same in two, and lower only in polar clouds, but the polar model overestimation could be due to underestimation of

TABLE 3. CMIP5 and CMIP6 model WS normalized RFO absolute deviation from the ISCCP-H WS (in %). The quantity is derived by averaging the absolute differences of model WS RFO from the ISCCP-H value and normalizing to the ISCCP-H value.

	DCN	MDS	CIR	PLR	MID	FRW	SHC	STC	AVG
CMIP6 (%)	21.4	20.9	49.8	69.8	35.8	12.12	48.9	34.9	36.7
CMIP5 (%)	52.2	31.6	24.6	67.7	44.0	19.4	39.7	45.5	40.6

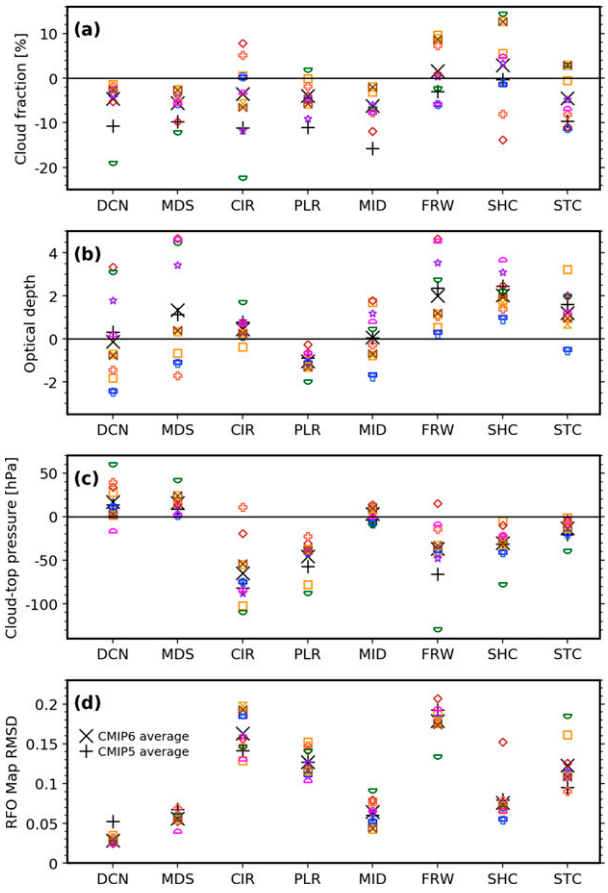

FIG. 8. Difference between CMIP6 model and ISCCP-H WS mean (a) cloud fraction, (b) cloud optical depth, and (c) cloud top pressure, and (d) root-mean-square difference between the WS RFO maps of the CMIP6 models and ISCCP-H. The CMIP6 model ensemble mean difference is indicated with an X and that for CMIP5 with a plus sign (+). CMIP6 model symbols are as indicated in Fig. 6.

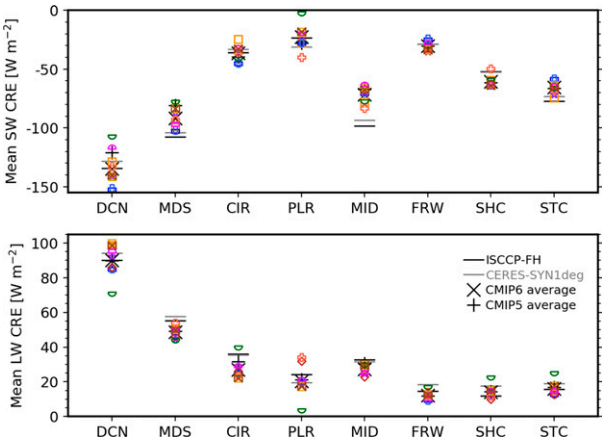

FIG. 9. Mean values of CMIP6 model WS (top) shortwave cloud radiative effect (SWCRE) and (bottom) longwave cloud radiative effect (LWCRE). The CMIP6 model ensemble mean is indicated with an X, the CMIP5 mean with a plus sign (+), and the mean values for the ISCCP-H WSs derived from the CERES and the ISCCP-FH radiative flux datasets are noted with horizontal bars. Model symbols are as indicated in Fig. 6. Positive (negative) values indicate radiative warming (cooling).

cloud optical depth in ISCCP retrievals over ice surfaces. The CMIP5 ensemble similarly has higher optical depth than ISCCP in most WSs. Overall, it can be said that CMIP6 models still follow the ''too few–too bright'' paradigm found in all previous generations of climate models (e.g., Webb et al. 2001; Weare 2004; Karlsson et al. 2008; Nam et al. 2012). The cloud top pressure of the deep convective and midlatitude storm WSs is larger than that found in ISCCP, implying generally lower cloud tops in the model simulations, while for most other WSs the cloud top pressures are generally lower than in ISCCP, indicating higher model cloud tops for cirrus, polar, and all low clouds. The bias for low cloud top pressures may be even worse because the ISCCP-H estimates seem to be biased low (Stubenrauch et al. 2013). Finally, the RFO geographical pattern differences between the CMIP6 model and ISCCP WSs are very small for deep convective, midlatitude storm, middle-top, and shallow cumulus WSs, meaning that the cloud types that are associated with the ITCZ and the midlatitude storm tracks show almost identical patterns with the observed ones. The cirrus and fair weather WSs, cloud types that tend to be more widespread, show the largest pattern differences from the observations. Note, however, that part of the difference in the pattern may represent differences in the RFO values between the model and ISCCP WSs. The WS pattern biases found in the present analysis are similar between the CMIP6 and CMIP5 ensembles and are both significantly smaller than the pattern differences found in a similar analysis of CMIP3 models by Williams and Webb (2009).

The distribution of shortwave and longwave cloud radiative effect (SWCRE and LWCRE) among the model weather states is evaluated in Fig. 9 against the observational distributions, derived from compositing the ISCCP-FH and CERES radiative flux data in the merged ISCCP-H weather states. The ISCCP-FH radiative flux retrievals are derived through the application of a radiative flux calculation on the ISCCP-H cloud field, and therefore they represent the radiative fluxes that the models would calculate if they faithfully simulated the ISCCP-H WS cloud property distributions. The difference between the ISCCP-FH and the CERES CRE values can be seen as the observational uncertainty, or even as the ISCCP-FH bias against the more direct CERES flux retrievals. Figure 9 shows that in all WS categories the observational uncertainty is much smaller than the model spread, and that in certain categories clear model biases can be identified. The largest model bias occurs in the middle top WS, where the model mean cloud shortwave cooling is too small by 20–30 W m^{-2}, due primarily to the underprediction of cloud fraction in that WS (cf. Fig. 8). A smaller SWCRE bias occurs in the midlatitude storm and the stratocumulus WSs, due to the underprediction of cloud fraction despite the overprediction of cloud optical depth in those categories. In contrast, SWCRE is too strong in shallow cumulus clouds, due to an overprediction of cloud cover and optical depth in

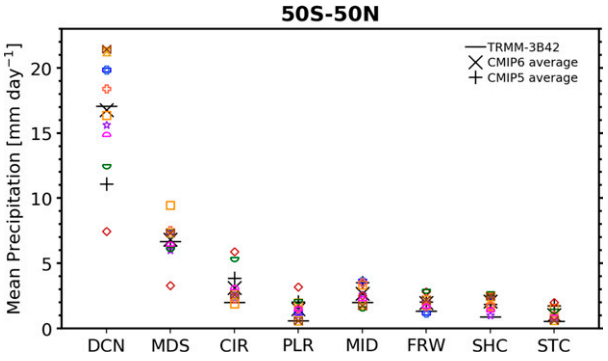

FIG. 10. Mean values of CMIP6 model WS precipitation. The CMIP6 model ensemble mean is indicated with an X, the CMIP5 mean with a plus sign (+), and the mean values for the ISCCP-H WSs derived from the TRMM precipitation dataset is noted with a horizontal bar. CMIP6 model symbols are as indicated in Fig. 6.

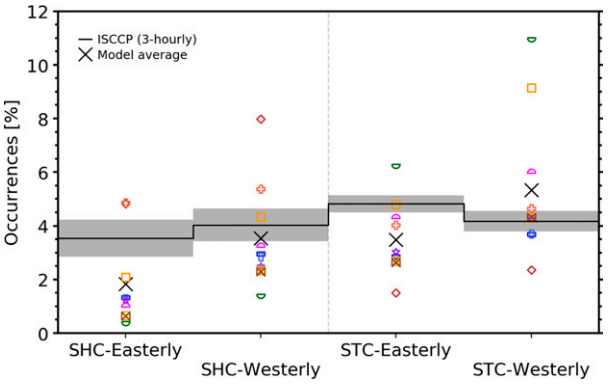

FIG. 11. Relative frequency of occurrence of the easterly and westerly components of the shallow cumulus (SHC) and stratocumulus (STC) WSs, from the ISCCP-H dataset (solid line) and the AMIP twentieth-century simulations of the CMIP6 models (model symbols are indicated in the label). The gray bar around the line indicates the ISCCP-H interannual variability. The X sign is the mean of each model ensemble.

those clouds. In the LWCRE evaluation, the only clear bias is in the midlatitude storm WS, where the lower model cloud tops and cloud fraction (Fig. 8) result in weaker LW cloud effects in all models. The somewhat weaker LW warming in the cirrus and middle-top WSs can only be explained by the lower cloud fraction in those regimes.

The distribution of precipitation among the model WS is evaluated in Fig. 10, against the same distribution from a composite of TRMM rain rate retrievals on the merged ISCCP-H weather states. The large majority of the observed precipitation falls in the deep convective and midlatitude storm WSs, with contributions from the cirrus (which may be due to platform space–time mismatch near convective systems) and the middle top WSs, and this distribution is present in the model simulations as well. However, CMIP6 models show a spread in precipitation rate in the deep convective and to a lesser extent the storm cloud WS that is very large, with the extreme models differing by as much as 10–15 mm day^{-1} in deep convective precipitation rates. In the ensemble mean, CMIP6 models simulate higher, more realistic convective precipitation rates than CMIP5 models. Also, all models tend to show a small overestimation of the low rain rates in all WSs other than the convective and storm cloud ones, indicating the presence of excess drizzle in the model simulations.

4. Discussion

A cluster analysis of TAU-PC histograms of the new, higher-resolution ISCCP-H dataset produces cloud regimes that are very similar to the lower-resolution ISCCP-D WSs. The main difference lies in the elimination of the ISCCP-D ''thin stratocumulus'' category and the splitting of those clouds between the stratocumulus and shallow cumulus ISCCP-H WSs. This happens because the ISCCP-H dataset resolves better the stratocumulus-to-shallow cumulus transition, while in the coarser ISCCP-D retrievals the mixed-cloud transition scenes are classified as a thin stratocumulus category. Another important difference is found in the polar cloud WS, which has a different, more consistent with the active retrievals TAU-PC distribution than the ISCCP-D one and is much better confined to the polar regions. The overall consistency between the two ISCCP WS analyses is indicative of the similarities between the two ISCCP datasets, with the differences coming mostly from the higher horizontal resolution of the ISCCP-H data and from the changes in the cloud property retrievals over ice-covered surfaces. This implies that results derived from analyses of the ISCCP-D WSs of Tselioudis et al. (2013) will remain consistent if the ISCCP-H WSs are used instead, unless polar clouds are the analysis focus.

The evaluation of the CMIP6 models against weather states derived from cloud property cluster analysis shows that in the ensemble average the models are producing an adequate representation of the frequency and geographical distribution of the WSs, with some improvements compared to the WSs derived for the CMIP5 ensemble. However, in some WSs like cirrus and stratocumulus, the good agreement of the model ensemble mean with the observations comes from averaging two groups of models that significantly overpredict and underpredict the RFO values. In addition, significant biases exist in the cloud properties of the model WSs, such as the model underestimation of cloud fraction in middle-top clouds and secondarily in midlatitude storm and stratocumulus clouds, that result in an underestimation of cloud shortwave cooling in those regimes. The cloud defined WSs constitute a useful framework to initiate a ''regime based'' evaluation of climate models.

As shown in the case of the boundary layer clouds, however, cloud distributions with similar radiative characteristics can still derive from distinct atmospheric processes. In the context of model evaluation and its use to improve cloud simulations, where knowledge of the mechanisms involved in cloud formation and dissipation is crucial, it may be necessary to further split the WSs to obtain consistent dynamic regimes. As an example, Fig. 11 shows the evaluation of the CMIP6 models separately for the RFO of the easterly and westerly components

of the SHC and STC WSs. It can be seen that for the SHC WS, which is underestimated in the whole by the models (Fig. 7), this underestimate is more pronounced in the tropical (easterly) than in the midlatitude (westerly) component of the WS. For the STC WS, which is slightly overestimated in the whole (Fig. 7), this overestimate comes from an underestimate of the tropical component and an overestimate of the midlatitude one. Overall, models tend to underpredict stratocumulus and shallow cumulus amounts in the tropical trade wind regime more than in the midlatitude cold air outbreak regime. This information provides additional insight into the processes that may be responsible for potential model cloud deficiencies, but further dynamical or thermodynamical compositing may be needed to meaningfully resolve cloud formation and dissipation processes.

As illustrated in Fig. 3 for the case of a midlatitude storm, the cluster analysis–derived WSs provide regime definitions that correspond to distinct combinations of dynamic and thermodynamic conditions that result in the formation of the distinct cloud type distributions. The evaluation of CMIP6 climate models using the WS distributions constitutes a meaningful regime-based evaluation, which can provide information pointing to the processes responsible for potential model deficiencies. Furthermore, if climate change is seen as a shift in the distribution of atmospheric regimes, then the ability of the models to reproduce the distribution of cloud, radiation, and precipitation properties among the regimes provides a test for their ability to simulate climate feedbacks resulting from atmospheric regime distribution shifts.

Acknowledgments. The research was supported by the NASA Making Earth System Data Records for Use in Research Environments (MEaSUREs) Program, under Grant 17-MEASURES-0034.

Data availability statement. The ISCCP-H Weather State dataset discussed in this study is available at http://isccp.giss.nasa.gov/wstates/hggws.html.

REFERENCES

Anderberg, M. R., 1973: *Cluster Analysis for Applications*. Elsevier, 359 pp.

Bodas-Salcedo, A., and Coauthors, 2011: COSP: Satellite simulation software for model assessment. *Bull. Amer. Meteor. Soc.*, **92**, 1023–1043, https://doi.org/10.1175/2011BAMS2856.1.

——, and Coauthors, 2014: Origins of the solar radiation biases over the Southern Ocean in CFMIP2 models. *J. Climate*, **27**, 41–56, https://doi.org/10.1175/JCLI-D-13-00169.1.

Bony, S., and J.-L. Dufresne, 2005: Marine boundary layer clouds at the heart of tropical cloud feedback uncertainties in climate models. *Geophys. Res. Lett.*, **32**, L20806, https://doi.org/10.1029/2005GL023851.

Dee, D. P., and Coauthors, 2011: The ERA-Interim reanalysis: Configuration and performance of the data assimilation system. *Quart. J. Roy. Meteor. Soc.*, **137**, 553–597, https://doi.org/10.1002/qj.828.

Ferraro, R., N. Grody, F. Weng, and A. Basist, 1996: An eight-year (1987–1994) time series of rainfall, clouds, water vapor, snow cover, and sea ice derived from SSM/I measurements. *Bull. Amer. Meteor. Soc.*, **77**, 891–905, https://doi.org/10.1175/1520-0477(1996)077<0891:AEYTSO>2.0.CO;2.

Grise, K. M., and B. Medeiros, 2016: Understanding the varied influence of midlatitude jet position on clouds and cloud radiative effects in observations and global climate models. *J. Climate*, **29**, 9005–9025, https://doi.org/10.1175/JCLI-D-16-0295.1.

Hansen, J., G. Russell, D. Rind, P. Stone, A. Lacis, S. Lebedeff, R. Ruedy, and L. Travis, 1983: Efficient three-dimensional global models for climate studies: Models I and II. *Mon. Wea. Rev.*, **111**, 609–662, https://doi.org/10.1175/1520-0493(1983)111<0609:ETDGMF>2.0.CO;2.

Huffman, G. J., and Coauthors, 2007: The TRMM Multisatellite Precipitation Analysis (TMPA): Quasi-global, multiyear, combined-sensor precipitation estimates at fine scales. *J. Hydrometeor.*, **8**, 38–55, https://doi.org/10.1175/JHM560.1.

Jakob, C., and G. Tselioudis, 2003: Objective identification of cloud regimes in the tropical western Pacific. *Geophys. Res. Lett.*, **30**, 2082, https://doi.org/10.1029/2003GL018367.

Jin, D., L. Oreopoulos, and D. Lee, 2017: Regime-based evaluation of cloudiness in CMIP5 models. *Climate Dyn.*, **48**, 89–112, https://doi.org/10.1007/s00382-016-3064-0.

Jin, Y., and W. B. Rossow, 1997: Detection of cirrus overlapping low-level clouds. *J. Geophys. Res.*, **102**, 1727–1737, https://doi.org/10.1029/96JD02996.

Karlsson, J., G. Svensson, and H. Rodhe, 2008: Cloud radiative forcing of subtropical low level clouds in global models. *Climate Dyn.*, **30**, 779–788, https://doi.org/10.1007/s00382-007-0322-1.

Lau, N., and M. W. Crane, 1995: A satellite view of the synoptic-scale organization of cloud properties in midlatitude and tropical circulation systems. *Mon. Wea. Rev.*, **123**, 1984–2006, https://doi.org/10.1175/1520-0493(1995)123<1984:ASVOTS>2.0.CO;2.

Loeb, N. G., and Coauthors, 2018: Clouds and the Earth's Radiant Energy System (CERES) Energy Balanced and Filled (EBAF) top-of-atmosphere (TOA) Edition-4.0 data product. *J. Climate*, **31**, 895–918, https://doi.org/10.1175/JCLI-D-17-0208.1.

Nam, C., S. Bony, J.-L. Dufresne, and H. Chepfer, 2012: The 'too few, too bright' tropical low-cloud problem in CMIP5 models. *Geophys. Res. Lett.*, **39**, L21801, https://doi.org/10.1029/2012GL053421.

Oreopoulos, L., N. Cho, D. Lee, S. Kato, and G. J. Huffman, 2014: An examination of the nature of global MODIS cloud regimes. *J. Geophys. Res.*, **119**, 8362–8383, https://doi.org/10.1002/2013JD021409.

Rémillard, J., and G. Tselioudis, 2015: Cloud regime variability over the Azores and its application to climate model evaluation. *J. Climate*, **28**, 9707–9720, https://doi.org/10.1175/JCLI-D-15-0066.1.

Rossow, W. B., 2017: ISCCP H-Version—Climate algorithm theoretical basis document. NOAA Climate Data Record Program (CDRP-ATDB-0.872) Rev 0 (2017). 301 pp., http://www1.ncdc.noaa.gov/pub/data/sds/cdr/CDRs/Cloud_Properties-ISCCP/AlgorithmDescription_01B-29.pdf.

——, and R. A. Schiffer, 1991: ISCCP cloud data products. *Bull. Amer. Meteor. Soc.*, **72**, 2–20, https://doi.org/10.1175/1520-0477(1991)072<0002:ICDP>2.0.CO;2.

——, G. Tselioudis, A. Polak, and C. Jakob, 2005: Tropical climate described as a distribution of weather states indicated by distinct mesoscale cloud property mixtures. *Geophys. Res. Lett.*, **32**, L21812, https://doi.org/10.1029/2005GL024584.

——, Y.-C. Zhang, and G. Tselioudis, 2016: Atmospheric diabatic heating in different weather states and the general circulation.

J. Climate, **29**, 1059–1065, https://doi.org/10.1175/JCLI-D-15-0760.1.

Schmidt, G. A., and Coauthors, 2006: Present-day atmospheric simulations using GISS ModelE: Comparison to in-situ, satellite and reanalysis data. *J. Climate*, **19**, 153–192, https://doi.org/10.1175/JCLI3612.1.

Somerville, R. C. J., and Coauthors, 1974: The GISS model of the global atmosphere. *J. Atmos. Sci.*, **31**, 84–117, https://doi.org/10.1175/1520-0469(1974)031<0084:TGMOTG>2.0.CO;2.

Stephens, G. L., D. G. Vane, and S. Tanelli, 2008: CloudSat mission: Performance and early science after the first year of operation. *J. Geophys. Res.*, **113**, 2156–2202, https://doi.org/10.1029/2008JD009982.

Stubenrauch, C. J., and Coauthors, 2013: Assessment of global cloud datasets from satellites: Project and database initiated by the GEWEX radiation panel. *Bull. Amer. Meteor. Soc.*, **94**, 1031–1049, https://doi.org/10.1175/BAMS-D-12-00117.1.

Tselioudis, G., and C. Jakob, 2002: Evaluation of midlatitude cloud properties in a weather and a climate model: Dependence on dynamic regime and spatial resolution. *J. Geophys. Res.*, **107**, 4781, https://doi.org/10.1029/2002JD002259.

——, W. Rossow, Y. Zhang, and D. Konsta, 2013: Global weather states and their properties from passive and active satellite cloud retrievals. *J. Climate*, **26**, 7734–7746, https://doi.org/10.1175/JCLI-D-13-00024.1.

Weare, B., 2004: A comparison of AMIP II model cloud layer properties with ISCCP D2 estimates. *Climate Dyn.*, **22**, 281–292, https://doi.org/10.1007/s00382-003-0374-9.

Webb, M., C. Senior, S. Bony, and J.-J. Morcrette, 2001: Combining ERBE and ISCCP data to assess clouds in the Hadley Centre, ECMWF and LMD atmospheric climate models. *Climate Dyn.*, **17**, 905–922, https://doi.org/10.1007/s003820100157.

Williams, K. D., and G. Tselioudis, 2007: GCM intercomparison of global cloud regimes: Present-day evaluation and climate change response. *Climate Dyn.*, **29**, 231–250, https://doi.org/10.1007/s00382-007-0232-2.

——, and M. J. Webb, 2009: A quantitative performance assessment of cloud regimes in climate models. *Climate Dyn.*, **33**, 141–157, https://doi.org/10.1007/s00382-008-0443-1.

Winker, D. M., and Coauthors, 2009: Overview of the CALIPSO mission and CALIOP data processing algorithms. *J. Atmos. Oceanic Technol.*, **26**, 2310–2323, https://doi.org/10.1175/2009JTECHA1281.1.

Young, A. H., K. R. Knapp, A. Inamdar, W. Hankins, and W. B. Rossow, 2018: The International Satellite Cloud Climatology Project H-series climate data record product. *Earth Syst. Sci. Data*, **10**, 583–593, https://doi.org/10.5194/essd-10-583-2018.